Post-Print

This is the accepted version of:

Autonomous Optical Navigation for the Lunar Meteoroid Impacts Observer

V. Franzese[*], P. Di Lizia[†], and F. Topputo[‡]
Politecnico di Milano, 20156, Milano, Via La Masa 34, Italy

I. Introduction

CubeSats are low-cost platforms to test innovative technologies in-flight that also allow performing science [1]. Adopting CubeSats is appealing due to the inherent savings in the design, production, and launch costs. While these costs scale with the mass, power, and size of the platforms, those related to operations do not obey the same trend. Navigation is among those operations that are performed routinely, regardless of the mission phase. Deep-space probes are usually navigated through ground-based radiometric tracking and orbit determination [2], which contribute significantly to the ground segment costs. Granting autonomous on-board navigation is instrumental to reducing the overall mission cost of small probes, and to pave the way for novel deep-space mission concepts [3].

The Lunar Meteoroid Impacts Observer, or LUMIO, is a 12U CubeSat mission to observe, quantify, and characterize the meteoroid impact flux by detecting their impact flashes on the lunar far-side [4]. LUMIO was awarded ex-aequo winner of the European Space Agency's challenge LUCE (Lunar CubeSat for Exploration), under the SysNova framework[§]. An independent assessment conducted at ESA's Concurrent Design Facility (CDF) has proven the mission feasible[¶], and as such LUMIO is currently being considered for future implementation.

LUMIO is placed in a quasi-halo orbit about Earth–Moon L_2 [5], as shown in Figure 1a–1b. From this orbit, full-disk images of the lunar farside are acquired through the LUMIO-Cam, an optical instrument capable of detecting meteoroid impact flashes in the visible spectrum. As a secondary application of the scientific investigation, the LUMIO-Cam is used to navigate autonomously, employing the Moon full-disk images to perform horizon-based navigation [6]. This technique resembles the backup navigation in Exploration Mission 1 [7]. The spacecraft state is estimated without relying on ground station tracking. Demonstrating this capability is the major technological objective of LUMIO.

This note describes the methods and tools developed to quantify the performances of the full-disk optical navigation in LUMIO. The horizon-based method [8] has been embedded into a simulator that generates synthetic Moon images via a ray tracer software. The position vector is then filtered to estimate the whole spacecraft state. Errors in the state, dynamics, and maneuver execution have been considered. Preliminary results show feasibility of the devised concept of operation for autonomous navigation and station keeping: requirements on position and velocity knowledge are satisfied.

---

[*]PhD Candidate, Department of Aerospace Science and Technology, Via La Masa 34, vittorio.franzese@polimi.it.
[†]Assistant Professor, Department of Aerospace Science and Technology, Via La Masa 34, pierluigi.dilizia@polimi.it. AIAA Member
[‡]Assistant Professor, Department of Aerospace Science and Technology, Via La Masa 34, francesco.topputo@polimi.it. AIAA Member.
[§]"CubeSats for Hunting Secrets in the Lunar Darkness"; see esa.int/Our_Activities/Space_Engineering_Technology (last accessed: May 2018).
[¶]"SysNova – Lunar Challenges Studied in the CDF"; see esa.int/Our_Activities/Space_Engineering_Technology/CDF (last accessed: May 2018).

(a) Lateral view (x, z).   (b) Front view (y, z).   (c) LUMIO concept of operations.
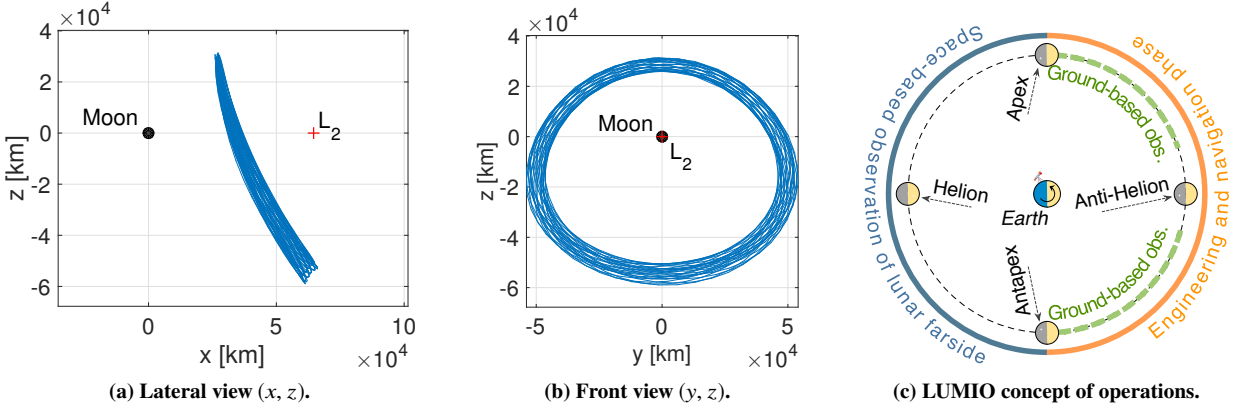
Fig. 1   LUMIO 1-year orbit: lateral view (a), front view (b); (c) LUMIO concept of operations.

## II. Background

A. Operative Orbit

LUMIO flies on a quasi-halo orbit around the L_2 point of the Earth–Moon system [9]. This orbit is resonant by a factor 2:1 with the Earth–Moon system: LUMIO performs approximately two revolutions about L_2 every Earth–Moon synodic period (29.48 days). This mechanism applies for the whole lifetime, which is one year. Considering two consecutive orbits, LUMIO will dedicate one orbit to engineering operations (e.g., station keeping), and the other one to science investigation (see Figure 1c). Figure 2 shows the LUMIO-to-Moon range and the angle between the LUMIO-Cam bore-sight and Sun (Moon–LUMIO–Sun angle) during three halo periods. These are the relevant geometrical quantities that mostly affect horizon-based optical navigation. The horizontal dashed line is the minimum exclusion angle between the LUMIO-Cam bore-sight and the Sun direction, that is 17.5 deg due to payload constraints mainly related to the LUMIO-Cam baffle. Relevant geometric and energetic parameters are given in Table 1.

Table 1   LUMIO halo orbit properties.

Min Range to Moon	Max Range to Moon	Halo Period	Earth-Moon Synodic Period	Jacobi Constant
35525 km	86551 km	14.74 days	29.48 days	3.09

B. Navigation Requirements

The navigation requirements for LUMIO are reported in Table 2. Each position and velocity vectors component shall be determined within an accuracy of 30 km and 50 cm/s, respectively, during the engineering orbit. A maximum acquisition frequency of 16.67 mHz (one update per minute) is set to balance on-board data processing for navigation purposes. LUMIO station keeping (S/K) operations require that 24 hours before each maneuver execution (cut-off time) position and velocity are known with an accuracy of 30 km and 30 cm/s, respectively. These requirements come from
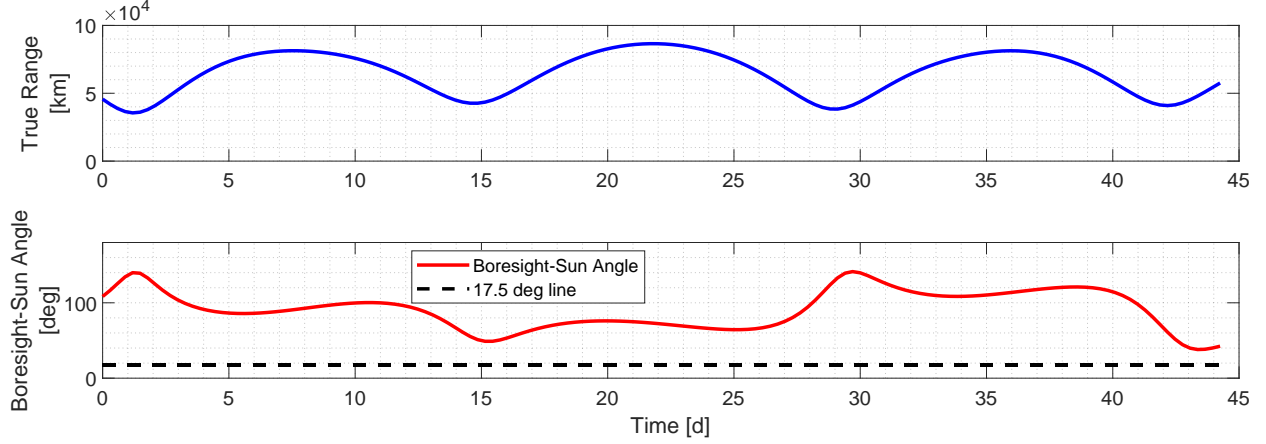
Fig. 2 LUMIO-to-Moon range and angle between LUMIO-Cam bore-sight and Sun direction.

the mission analysis, and guarantee that the total 1-year S/K cost is below 18 m/s, which is the allocated budget [5].

Table 2 LUMIO mission navigation requirements on components of position, velocity.

Engineering Orbit			Station Keeping		
3σ **position**	3σ **velocity**	**Max freq.**	3σ **position**	3σ **velocity**	**Cut-off time**
30 km	50 cm/s	16.67 mHz	30km	30 cm/s	24 h

C. Navigation Techniques Trade-Off

The considered navigation techniques for the trade-off are the radiometric tracking [2], the X-ray pulsar navigation [10, 11], the Celestial Triangulation [12, 13] and the Horizon-Based navigation [8, 14–16]. Evaluation criteria such as autonomy, accuracy, sensor maturity, and cost, are traded-off in Table 3. The objective of demonstrating the feasibility of autonomous on-board navigation excludes ground-based radiometric navigation as baseline for LUMIO. The X-ray Pulsar navigation, among the most promising navigation methods [10], still requires huge developments for CubeSats implementation due to sensor miniaturization constraints. Viable navigation techniques for LUMIO are then Celestial Triangulation and Horizon-Based navigation. The Celestial Triangulation method would employ the star trackers and the LUMIO-Cam to acquire the line of sight directions of known celestial objects (e.g., Earth, Moon) and triangulate the CubeSat position [13]; the Horizon-Based navigation would instead directly use images of the Moon full disk to estimate the current spacecraft position [8]. Both methods require the celestial objects ephemeris as well as LUMIO attitude to be known. The Horizon-Based navigation has been selected as baseline for LUMIO and is preferred to the Celestial Triangulation for the higher accuracy, since the Moon occupies a large portion of the LUMIO-Cam field of view at the given distances, and its full-disk is always visible.

Table 3   Navigation techniques trade-off.

	Autonomy	Accuracy	Sensor	Cost
Radiometric Tracking	Not Autonomous	Order of m	Mature	High
X-ray Pulsar Navigation	Autonomous	Order of km	Not Ready	N. A.
Celestial Optical Triangulation	Autonomous	Order of 10^3 km	Mature	Low
Horizon-Based Optical Navigation	Autonomous	Order of 10^2 km	Mature	Low

☐ Meets requirements   ☐ Correctable deficiencies   ■ Unacceptable

D. Overview of Horizon-Based Optical Navigation

A viable solution to the Horizon-Based Optical navigation problem when observing a moon or a planet has been proposed in [8, 14, 15]. It is valid when the observed body can be modeled as a tri-axial ellipsoid with shape matrix $A = \text{diag}\left(a^{-2}, b^{-2}, c^{-2}\right)$, where a, b, and c are the semi-axis lengths of the tri-axial ellipsoid. The formulation in [8] is applied to the LUMIO mission case. The goal of the Horizon-Based navigation is to estimate a camera-to-object relative position vector in the camera reference frame (defined as a right-handed frame having two axes belonging to the camera plane and the third axis aligned with the camera bore-sight) from the line-of-sight directions to some object full-disk points. The object full-disk is estimated by fitting an ellipse to the observed lit horizon points, which are retrieved from 2D images. The solution to the navigation problem is [8]

$$r = -U^{-1}(n^T n - 1)^{-1/2} n, \tag{1}$$

where r is the camera-to-object position vector in the camera reference frame, U the Cholesky decomposition of the ellipsoid shape matrix A ($A = U^T U$), and n the solution to the least-squares problem

$$Cn = \mathbf{1}_{m \times 1}, \tag{2}$$

C being the rectangular matrix collecting all the line of sight directions from the camera to the object full-disk points expressed into the Cholesky space, and $\mathbf{1}_{m \times 1}$ a vector of unitary values of size m, the number of full-disk points employed for navigation. The geometry of the camera-to-Moon line-of-sight directions composing the C matrix can be seen in Figure 3 in [8], where the complete formulation of the horizon-based navigation can be found as well. An equivalent but more computationally efficient solution adopting the singular value decomposition of A can be found in [17].

III. Simulation of the Autonomous Navigation

The application of the horizon-based optical navigation for LUMIO is simulated by generating and processing synthetic images of the Moon. The performances are then assessed and verified against the navigation requirements in
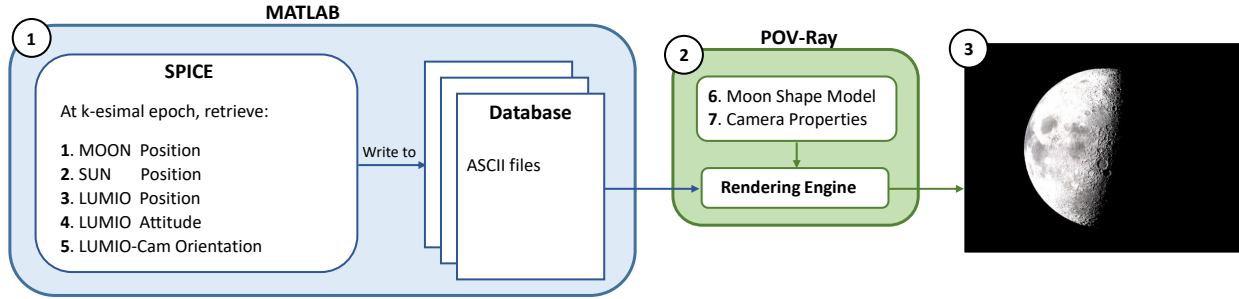
Fig. 3 Image generation: 1) Geometry definition; 2) Observation properties; 3) Rendered image.

Table 2. The overall process implemented to simulate LUMIO autonomous navigation consists of: 1) The generation of synthetic Moon images with a rendering software (Section III.A); 2) The processing of these images for horizon-based navigation (Section III.B); and, 3) The determination of the spacecraft state via extended Kalman filter (Section III.C).

A. Moon Images Generation

The software POV-Ray* is used to generate synthetic images of the Moon. The POV-Ray engine can render an image of a modeled object as captured by an user-defined camera once the geometry as well as the camera properties are defined. The image simulator developed is a combination of MATLAB and POV-Ray, and its high-level architecture is shown in Figure 3. The generation of synthetic images of the Moon is performed through the following steps:

1) In MATLAB, the positions of LUMIO, the Moon, and the Sun are retrieved as function of the epoch, along with the LUMIO attitude and LUMIO-Cam orientation. These data are provided by SPICE[†] kernels and are exported into ASCII files.

2) In POV-Ray, the Moon is modeled by creating a 3D object resembling the real Moon size, with the Moon texture and the Moon digital elevation map[‡]. The LUMIO-Cam properties are set by using the values in Table 4. The data from point 1) are used to define the LUMIO-Moon-Sun geometry.

3) The POV-Ray engine reads parameters from 1) and 2) and renders the Moon image to be used for navigation.

Table 4 LUMIO-Cam properties.

| Resolution	Field Of View	Focal Length	Pixel Size
1024x1024 pixels	6.0 deg	127 mm	13 μm

Simulating the continuous acquisition of images by the LUMIO-Cam is done by a recurrent application of the method in Figure 3 for varying epoch. In Figure 4, sample synthetic images of the Moon as seen from the LUMIO operative orbit (Section II.A) are shown. These are 8 out of 100 total simulated images. Note that the actual LUMIO-to-Moon

---

*Persistence of Vision Raytracer (POV-Ray), Williamstown, Australia. Retrieved from www.povray.org (last accessed: May 2018).
[†]NASA's Observation Geometry and Information System for Space Science Missions [18, 19]; naif.jpl.nasa.gov/naif (last accessed: May 2018).
[‡]Retrieved from Lunar Reconnaissance Orbiter database: astrogeology.usgs.gov (last accessed: May 2018).

range and the LUMIO–Moon–Sun geometry during the orbit cause the Moon size and surface illumination to vary.
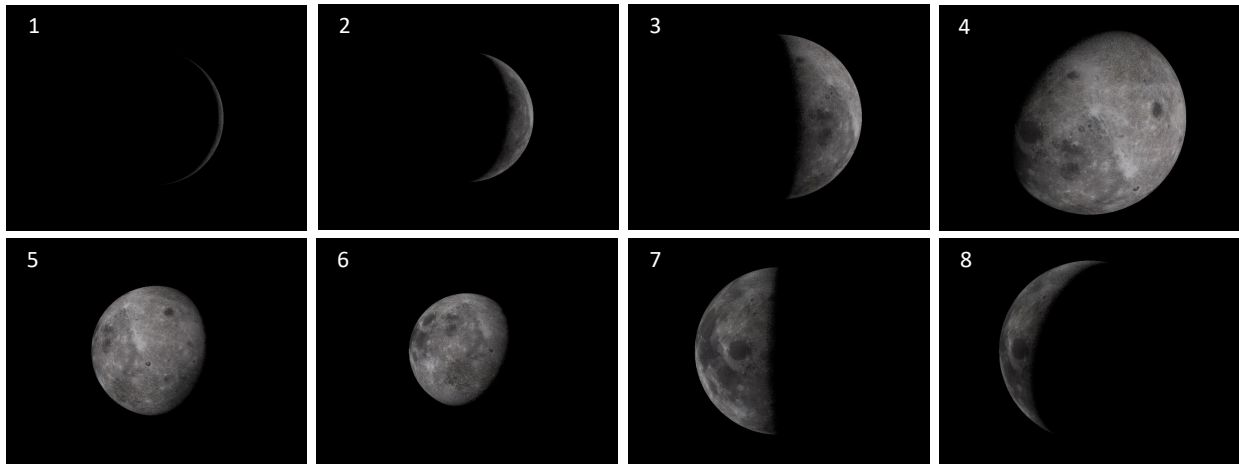
Fig. 4   Sample Moon images simulated.

B. Image Processing

The synthetic raw images acquired by the LUMIO-Cam are post-processed to detect the Moon horizon. The aim of the image processing algorithm is to obtain precise position coordinates of the celestial object lit horizon line in the camera reference frame. An ellipse is fitted to the Moon horizon points to reconstruct the Moon full-disk (Figure 5). The line of sight directions from the camera to the Moon full-disk can then be retrieved, and are used to estimate the relative camera-to-Moon position following the horizon-based optical navigation (see Section II.D).
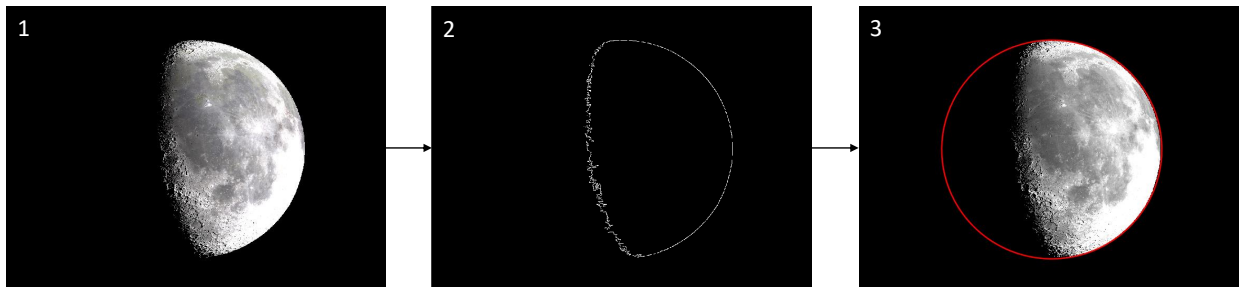
Fig. 5   Lunar images processing: 1) Image Acquisition; 2) Edge Finding; 3) Full Disk Estimation.

Algorithm 1 describes the image processing steps [14]. The acquired image is converted first into black and white according to a given threshold. A filter removes the background noise and the Moon contour is obtained with edge finding methods (e.g., Canny method [20]). The latter requires the light direction, which is assumed to be known (e.g., either through star trackers or deduced directly by the image [15]). The image can then be rotated with a bilinear interpolation algorithm such that the light direction is downward. It is scanned from top to bottom such that the first illuminated pixel is an horizon pixel. The pixels below the horizon one are discarded, and the image is rotated back once every column has been scanned. An ellipse, representing the celestial body full-disk, is fit to the newly found lit

horizon points. The ellipse coordinates are saved and later used for the relative camera-to-object position estimation (Section II.D), which feed the orbit determination filtering (Section III.C). This is a preliminary method to detect the Moon horizon in images; more accurate algorithms exists [15, 17].

Algorithm 1 Moon images processing

---

    loop on image k
        1. Convert image to black and white
        2. Remove background noise
        3. Obtain light direction and scan image
        4. Obtain Moon horizon points
        5. Fit ellipse to horizon points
    end loop

C. Orbit Determination

The output of image processing is the camera-to-Moon position estimation in the camera reference frame, yet no information on spacecraft velocity is available. An extended Kalman filter (EKF) [21] is then used to estimate the spacecraft state (position and velocity), to increase the navigation accuracy.

Algorithm 2 Extended Kalman filter implementation

System

1: $x_k = f(x_{k-1}, w_{k-1})$;
2: $y_k = H x_k + v_k$;

Noise

3: $w_k \sim (0, Q_k)$;
4: $v_k \sim (0, R_k)$;

Initialization

5: $\hat{x}_0^+ = E[x_0]$;
6: $P_0^+ = E[(x_0 - \hat{x}_0^+)(x_0 - \hat{x}_0^+)^T]$;

Filter

7: **for** k = 1,...,end **do**

     Prediction:
8:    $\hat{x}_k^- = f(\hat{x}_{k-1}^+)$;
9:    $P_k^- = F_{k-1}P_{k-1}^+ F_{k-1}^T + Q_{k-1}$;

     Correction:
10: $K_k = P_k^- H^T (H P_k^- H^T + R_k)^{-1}$;
11: $\hat{x}_k^+ = \hat{x}_k^- + K_k [y_k - H \hat{x}_k^-]$;
12: $P_k^+ = (I - K_k H) P_k^-$;

13: **end for**

The EKF implementation is summarized in Algorithm 2, where x is the 6x1 spacecraft state vector expressed in the J2000 reference frame centered at the Moon, f is the right-hand side of the astrodynamics model [22], y is the camera-to-Moon position measurement expressed in the J2000 frame, $H = [I_{3x3}, 0_{3x3}]$, P is the state estimate error covariance, F is $\partial f / \partial x$, K is the Kalman gain, and k represents the discrete step. The model and measurement errors, w and v, respectively, are mutually uncorrelated zero-mean white noise processes with known covariances (Q and R, respectively). The "^" superscript denotes estimated quantities, while "+" and "−" are used for predicted and corrected quantities, respectively. The filter settings are shown in Section IV.C.

IV. Navigation Performances

A. Concept of Operation

LUMIO performs three S/K maneuvers during each engineering operations orbit. The autonomous S/K requires that 24 hours before the maneuver execution (cut-off time) the 3σ knowledge on each position component is below 30 km and the 3σ knowledge on each velocity component is below 30 cm/s (see Table 2). The station keeping planning for LUMIO is shown in Figure 6a, where three orbits are shown, the first and the third being those devoted to engineering and navigation; the vertical dashed lines mark the halo periods, the maneuver execution time is indicated with a circle, and the stars indicate the cut-off time to meet the navigation requirements. Before the cut-off times, the images acquisition frequency is increased to refine the state estimation, while housekeeping acquisition frequencies are set for the remaining part of the orbits, as shown in Figure 6b. The rationale is as follows:

1) A High Frequency of 1 acquisition per minute (HF = 16.7 mHz) is used one day before the cut-off times;

2) A Medium Frequency of 1 acquisition per 10 minutes (MF = 1.67 mHz) is employed during nominal operations;

3) A Low Frequency of 1 acquisition per 60 minutes (LF = 0.277 mHz) is used during the science orbit.
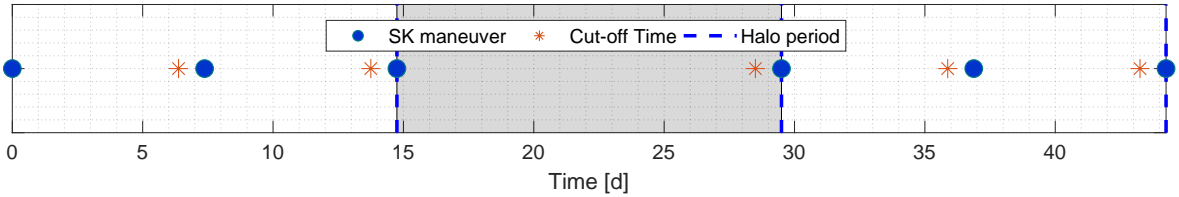
(a) S/K for LUMIO: three maneuvers are executed during each engineering orbit, while no maneuvers are executed during the science orbit.
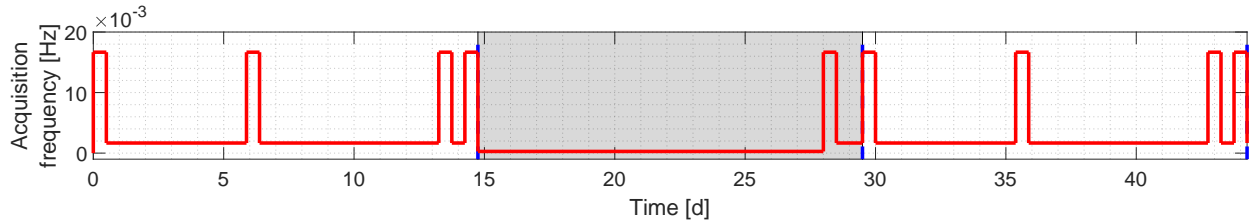
(b) Acquisition frequencies tuning: HF before S/K cut off, MF during engineering and navigation orbit, LF during science orbit.

Fig. 6 Station keeping planning and acquisition frequencies tuning for LUMIO mission (science orbit in grey).

B. Position Estimation from Image Processing

A set of images has been generated with the simulator shown in Section III.A to test the LUMIO optical navigation. The static navigation error is shown in Figure 7 for the same three halo orbits in Figure 6. This error accounts for the instantaneous position vector estimation by image processing without filtering, and is expressed in the camera reference frame, where x, y, and z are the left, up, and depth directions, respectively [8]. The root mean squared error (RMSE) is

computed as

$$\text{RMSE} = \sqrt{\frac{\sum_{i=1}^{N} p_i^2}{N}},\tag{3}$$

where p_i is a position component error at the epoch i, and N is the total number of measurements. With the values in Figure 7, the maximum error is RMSE = 83.60 km. This value, which corresponds to the 1σ standard deviation for an unbiased estimator, is used to characterize the white noise processes in the Kalman filter in Section IV.C.
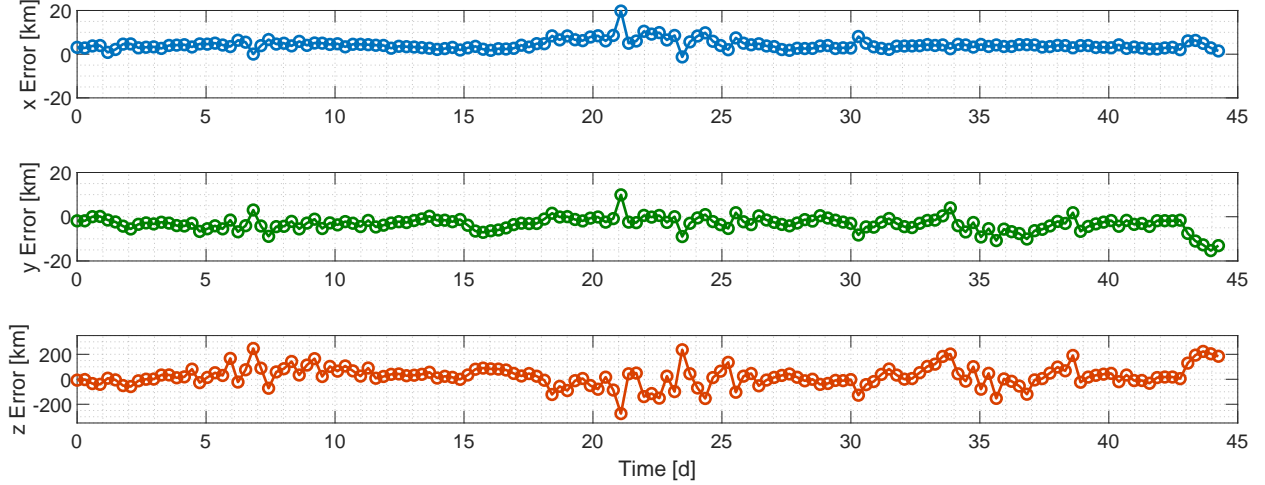
Fig. 7   LUMIO position error in the camera reference frame.

C. Extended Kalman Filter Implementation

The settings for the extended Kalman filter are shown in Table 5.

Table 5   Extended Kalman filter settings.

P_0 (km^2, km^2/s^2)	Q (km^2, km^2/s, km^2/s^2)	R (km^2)	HF	MF	LF
$\begin{bmatrix} 10^4\,I_3 & 0_3 \\ 0_3 & 10^{-6}\,I_3 \end{bmatrix}$	$10^{-12}\,1_{6\times6}$	$7.0\times10^3\,I_3$	0.0167 Hz	0.00167 Hz	0.000277 Hz

The measurements for the extended Kalman filter are zero-mean white noise processes, expressed in the J2000 reference frame originated in the Moon barycenter, and a 3σ standard deviation of 250.8 km has been attributed to each position vector component (X, Y, and Z). This is consequent to the results in Section IV.B, where the maximum RMSE is 83.60 km. In this way, all the possible errors coming from image processing are included. Note that more accurate measurement noise covariance models exist [23, 24].

D. Filter Outputs

Figure 8 shows the three position components residuals and the 3σ bounds after the filtering action. The dashed vertical lines mark the halo periods, while the gray and black lines are the measurement noise and the filtered error for each position component, respectively. The 3σ bounds for each position components are also shown. The 3σ bounds in the position estimation are compliant with the requirements in Table 2, with a position error that is kept within 30 km during engineering operations.
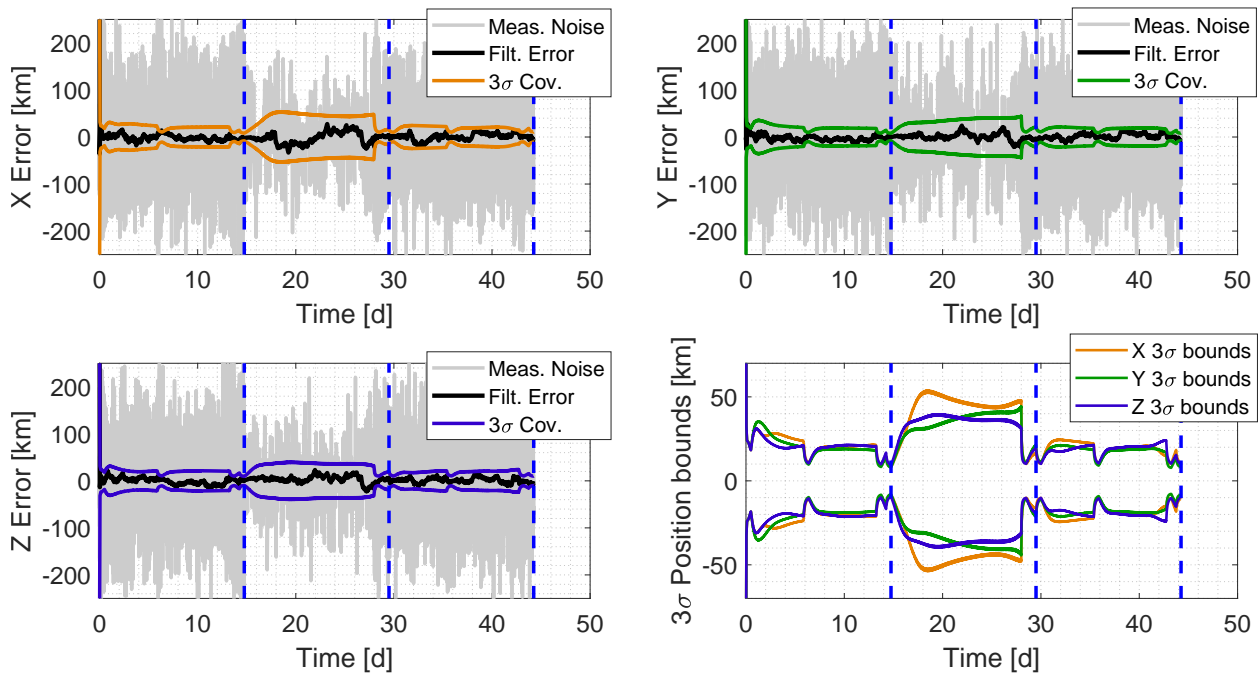
Fig. 8   EKF output error for each position component with related 3σ bounds.

The relation between station keeping planning, acquisition frequency and filter output is illustrated in Figure 9. Three station keeping maneuvers are planned each engineering operations orbit, namely at the beginning, at the middle, and at the end of the engineering orbit. Accurate position information is required 24 hours before the maneuvers execution. Accordingly, HF = 16.7 mHz is employed to minimize the position error at the S/K cut-off time. During nominal engineering operations, MF = 1.67 mHz is used to satisfy the navigation requirements in Table 2, while LF = 0.277 mHz is used in the scientific orbit to keep the position error bounded.

The estimation of the velocity components, which are not directly obtained from image processing, is reported in Figure 10. The adopted acquisition frequencies allow keeping the velocity error within the bounds expressed in Table 2; i.e., 50 cm/s for each component during operations phase and 30 cm/s at the S/K cut-off time. A Monte Carlo campaign has been executed with 100 initial states generated by sampling $\boldsymbol{P}_0$ as in Table 5. The resulting position and velocity error profiles lie within the mean 3σ covariance bounds predicted by the filter across all the runs, as shown in Figure 11. To check the consistency of the covariance estimation, Figure 11 also reports the sample covariance, computed from the
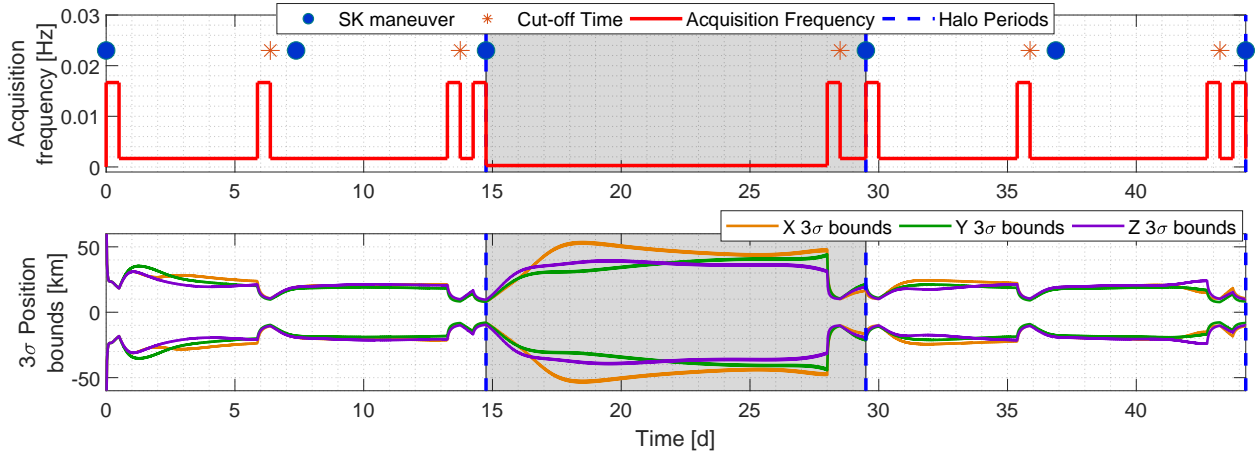
Fig. 9   Relations between LUMIO conops, acquisition frequency, and position error bounds (3σ) after filtering.
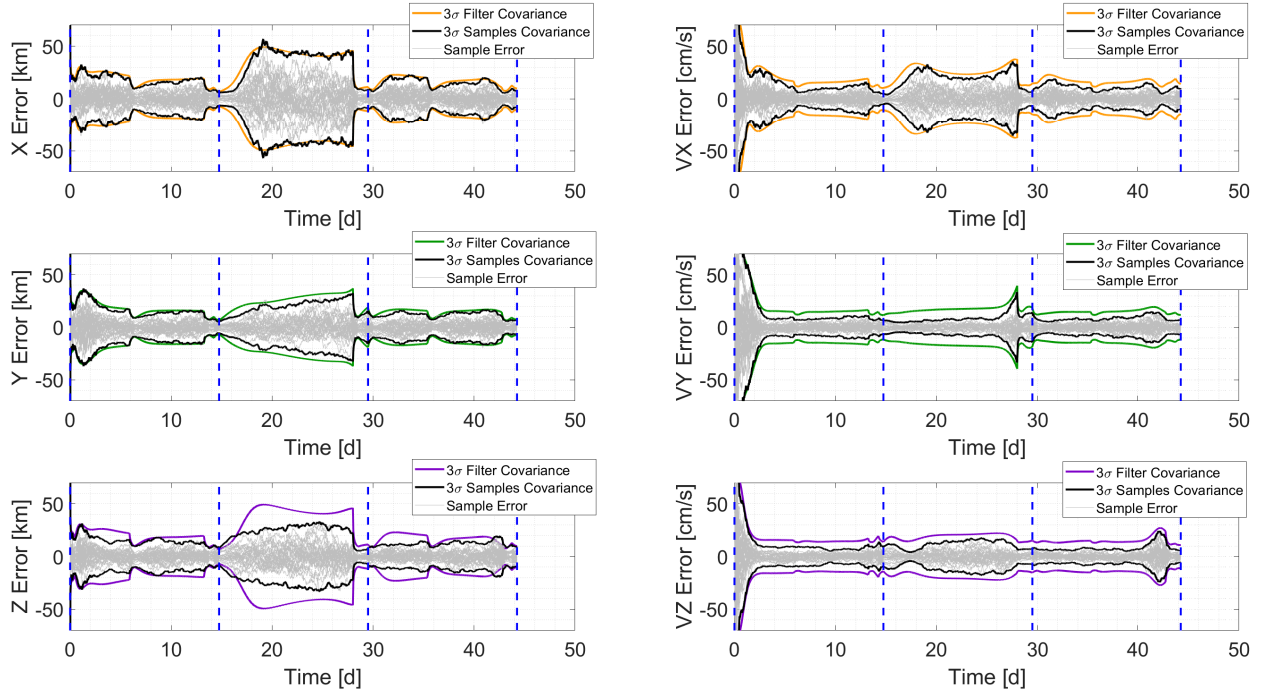
history of the Monte Carlo samples.

V. Conclusions

The feasibility of autonomous optical navigation for LUMIO, a CubeSat mission at Earth–Moon L_2, has been investigated. To this purpose, an image simulator has been developed by combining MATLAB, SPICE, and POV-Ray to generate synthetic renderings of the Moon. An extended Kalman filter has been adopted to process the information obtained from image processing. By a proper definition of the concept of operation and a variable image acquisition
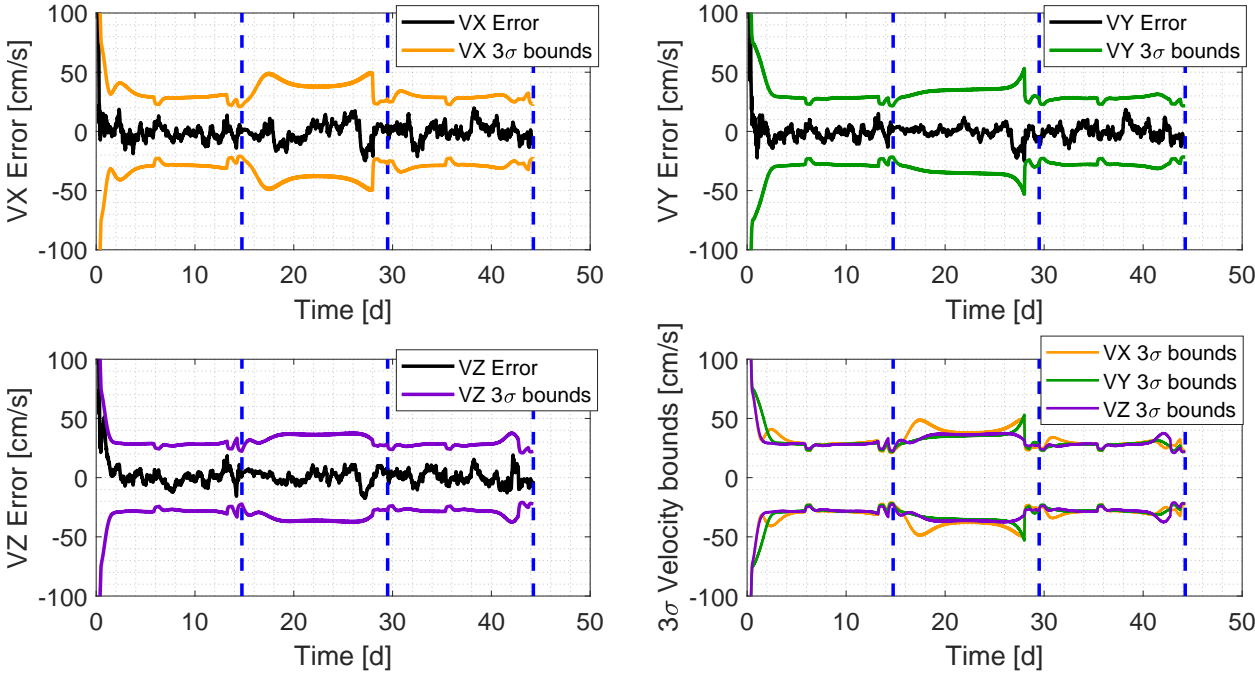
Fig. 10   EKF output error for each velocity component with related 3σ bounds.

Fig. 11   Comparison between the mean filter covariance (colored) and the sample covariance (black) on the six state components. For clarity sake, only 30 out of 100 Monte Carlo sample histories are reported (grey).

frequency policy, it has been shown that navigation requirements are met. The results in terms of position and velocity components residuals and covariance bounds confirm the preliminary feasibility of autonomous optical navigation for the LUMIO mission.

Acknowledgments

References

[1] Poghosyan, A., and Golkar, A., "CubeSat evolution: Analyzing CubeSat capabilities for conducting science missions," *Progress in Aerospace Sciences*, Vol. 88, 2017, pp. 59–83. doi:10.1016/j.paerosci.2016.11.002.

[2] Thornton, C. L., and Border, J. S., *Radiometric Tracking Techniques for Deep Space Navigation*, John Wiley & Sons, 2003, Chap. 2. doi:10.1002/0471728454.

[3] Quadrelli, M. B., Wood, L. J., et al., "Guidance, navigation, and control technology assessment for future planetary science missions," *Journal of Guidance, Control, and Dynamics*, Vol. 38, No. 7, 2015, pp. 1165–1186. doi:10.2514/1.G000525.

[4] Topputo, F., Massari, M., Biggs, J., et al., "LUMIO: a Cubesat at Earth-Moon L2," *4S Symposium*, 2018, pp. 1–15. URL http://hdl.handle.net/11311/1055454.

[5] Speretta, S., Topputo, F., et al., "LUMIO: achieving autonomous operations for Lunar exploration with a CubeSat," *2018 SpaceOps Conference*, 2018, p. 2599. doi:10.2514/6.2018-2599.

[6] Franzese, V., Di Lizia, P., and Topputo, F., "Autonomous Optical Navigation for LUMIO Mission," *2018 Space Flight Mechanics Meeting, AIAA SciTech Forum, (AIAA 2018-1977)*, 2018, pp. 1–11. doi:10.2514/6.2018-1977.

[7] Holt, G. N., D'Souza, C. N., and Saley, D. W., "Orion Optical Navigation Progress Toward Exploration Mission 1," *2018 Space Flight Mechanics Meeting, AIAA SciTech Forum, (AIAA 2018-1978)*, 2018, pp. 1–12. doi:10.2514/6.2018-1978.

[8] Christian, J. A., and Robinson, S. B., "Noniterative Horizon-Based Optical Navigation by Cholesky Factorization," *Journal of Guidance, Control, and Dynamics*, Vol. 39, No. 12, 2016, pp. 2757–2765. doi:10.2514/1.G000539.

[9] Cipriano, A., Dei Tos, D. A., and Topputo, F., "Orbit Design for LUMIO: The Lunar Meteoroid Impacts Observer," *Frontiers in Astronomy and Space Sciences*, Vol. 5, 2018, pp. 1–23. doi:10.3389/fspas.2018.00029.

[10] Sheikh, S. I., Pines, D. J., Ray, P. S., , et al., "Spacecraft Navigation Using X-Ray Pulsars," *Journal of Guidance, Control, and Dynamics*, Vol. 29, No. 1, 2006, pp. 49–63. doi:10.2514/1.13331.

[11] Anderson, K., Pines, D., and Sheikh, S., "Validation of pulsar phase tracking for spacecraft navigation," *Journal of Guidance, Control, and Dynamics*, Vol. 38, No. 10, 2015, pp. 1885–1897. doi:10.2514/1.G000789.

[12] Karimi, R., and Mortari, D., "Interplanetary Autonomous Navigation Using Visible Planets," *Journal of Guidance, Control, and Dynamics*, Vol. 38, No. 6, 2015, pp. 1151–1156. doi:10.2514/1.G000575.

[13] Mortari, D., and Conway, D., "Single-point position estimation in interplanetary trajectories using star trackers," *Advances in the Astronautical Sciences*, Vol. 156, No. 1, 2016, pp. 1909–1926. doi:10.1007/s10569-016-9738-4.

[14] Christian, J. A., "Optical Navigation Using Iterative Horizon Reprojection," *Journal of Guidance, Control, and Dynamics*, Vol. 39, No. 5, 2016, pp. 1092–1103. doi:10.2514/1.G001569.

[15] Mortari, D., D'Souza, C. N., and Zanetti, R., "Image processing of illuminated ellipsoid," *Journal of Spacecraft and Rockets*, 2016, pp. 448–456. doi:10.2514/1.A33342.

[16] Borissov, S., and Mortari, D., "Centroiding and Sizing Optimization of Ellipsoid Image Processing using Nonlinear Least-Squares," *Paper AAS 18-229, 2018 AAS/AIAA Astrodynamics Specialist Conference*, Snowbird, UT, August 19-23, 2018, pp. 1–14.

[17] Christian, J. A., "Accurate planetary limb localization for image-based spacecraft navigation," *Journal of Spacecraft and Rockets*, Vol. 54, No. 3, 2017, pp. 708–730. doi:10.2514/1.A33692.

[18] Acton, C. H., "Ancillary data services of NASA's navigation and Ancillary Information Facility," *Planetary and Space Science*, Vol. 44, No. 1 SPEC. ISS., 1996, pp. 65–70. doi:10.1016/0032-0633(95)00107-7.

[19] Acton, C., Bachman, N., Semenov, B., and Wright, E., "A look towards the future in the handling of space science mission geometry," *Planetary and Space Science*, Vol. 150, No. February 2017, 2018, pp. 9–12. doi:10.1016/j.pss.2017.02.013.

[20] Canny, J., "A Computational Approach to Edge Detection," *IEEE Transactions on Pattern Analysis and Machine Intelligence*, 1986, pp. 679–689. doi:10.1109/TPAMI.1986.4767851.

[21] Simon, D., *Optimal state estimation: Kalman, H infinity, and nonlinear approaches*, John Wiley & Sons, 2006, Chap. 13.

[22] Dei Tos, D. A., and Topputo, F., "Trajectory refinement of three-body orbits in the real solar system model," *Advances in Space Research*, Vol. 59, No. 8, 2017, pp. 2117–2132. doi:10.1016/j.asr.2017.01.039.

[23] Hikes, J., Liounis, A. J., and Christian, J. A., "Parametric covariance model for horizon-based optical navigation," *Journal of Guidance, Control, and Dynamics*, Vol. 40, No. 1, 2017, pp. 170–178. doi:10.2514/1.G000708.

[24] Enright, J., Jovanovic, I., Kazemi, L., Zhang, H., and Dzamba, T., "Autonomous optical navigation using nanosatellite-class instruments: a Mars approach case study," *Celestial Mechanics and Dynamical Astronomy*, Vol. 130, No. 2, 2018, pp. 1–31. doi:10.1007/s10569-017-9800-x.